RSC Advances

PAPER

View Article Online
View Journal | View Issue

Cite this: *RSC Adv.*, 2025, **15**, 47587

DOPO-functionalized Fe-based metal–organic framework and its synergistic flame retardant effect with microencapsulated ammonium polyphosphate in epoxy composites

Nhung Hac Thi,[ab] Hong Tham Nguyen,[a] Duc Long Tran,[a] Ho Thi Oanh,[a] Tien Dat Doan,[a] Giang Le Nhat Thuy,[a] Ha Tran Nguyen,[cd] Tuyen Van Nguyen[ab] and Mai Ha Hoang*[ab]

A novel hybrid flame-retardant system, named MOF-DOPO, was developed by chemically grafting 9,10-dihydro-9-oxa-10-phosphaphenanthrene-10-oxide (DOPO) to an Fe-based metal–organic framework (Fe-MOF-NH_2). The combination of MOF-DOPO and urea–melamine–formaldehyde microencapsulated ammonium polyphosphate (APP@UMF) markedly enhanced the fire resistance of epoxy resin. Comprehensive analyses indicated a synergistic flame-retardant mechanism between MOF-DOPO and APP@UMF operating in both gas and condensed phases. In the gas phase, phosphorus-centered radicals from DOPO effectively captured flame-propagating radicals, while nonflammable gases (NH_3, CO_2, H_2O) diluted and cooled the combustion zone. In the condensed phase, a compact intumescent char reinforced by thermally stable iron phosphate species ($Fe_2P_2O_7$, $Fe_2P_4O_{12}$, $Fe(PO_3)_2$) served as an efficient physical barrier to heat and mass transfer. Moreover, the formation of the spherical particulate network of iron phosphate species covering the surface of the burning material imparted a "lotus-leaf effect", minimizing flame impingement and retarding further degradation. Additionally, the incorporation of MOF-DOPO significantly mitigated the mechanical deterioration induced by APP@UMF. This study provides a feasible and effective strategy for developing epoxy nanocomposites with superior flame retardancy and good mechanical properties.

Received 18th October 2025
Accepted 26th November 2025

DOI: 10.1039/d5ra07990j

rsc.li/rsc-advances

1. Introduction

Epoxy resin (EP) is widely used in coatings, adhesives, electronic encapsulation, and composites, owing to its excellent thermal stability, high mechanical strength, good chemical resistance, and strong adhesion.[1–3] However, EP is inherently flammable and releases dense smoke and toxic gases during combustion, severely restricting its applications in fields requiring high fire safety.[4] Hence, developing effective flame-retardant strategies for EP is of great importance.

Among various approaches, intumescent flame retardants (IFRs) have gained increasing attention as halogen-free additives due to their high efficiency, low smoke emission, and environmental safety.[5–10] IFRs act by generating an intumescent carbonaceous char layer that insulates the polymer from heat and oxygen. Ammonium polyphosphate (APP), a typical acid source in IFR systems, promotes char formation through the production of phosphoric species during thermal decomposition.[11–14] Nevertheless, pristine APP suffers from poor interfacial compatibility with epoxy, which can impair mechanical performance. To overcome these limitations, considerable research has focused on improving the interfacial compatibility of APP *via* surface modification, and microencapsulation is a feasible and effective method. APP has been successfully modified using hyperbranched polyethyleneimine,[15,16] tannic acid,[17] phosphorus-containing silane coupling agents.[18,19] Meanwhile, melamine formaldehyde (MF),[20–22] urea formaldehyde,[23] polyvinyl alcohol-MF,[24] and urea-MF[25–27] resins can be used to encapsulate APP effectively.

In recent years, the incorporation of metal–organic frameworks (MOFs) as multifunctional flame-retardant synergists has attracted considerable attention owing to their unique structural and physicochemical properties, including tunable structure, large surface area, high porosity, diverse metal–ligand composition, and scalable functionality.[28–32] In particular, Fe-

---

[a] *Institute of Chemistry, Vietnam Academy of Science and Technology, 18 Hoang Quoc Viet, Nghia Do, Ha Noi, 10000, Vietnam. E-mail: hoangmaiha@ich.vast.vn*

[b] *Graduate University of Science and Technology, Vietnam Academy of Science and Technology, 18 Hoang Quoc Viet, Nghia Do, Ha Noi, 10000, Vietnam*

[c] *National Key Laboratory of Polymer and Composite Materials, Vietnam National University Ho Chi Minh City, 268 Ly Thuong Kiet, Dien Hong, Ho Chi Minh City, 70000, Vietnam*

[d] *Ho Chi Minh City University of Technology, Viet Nam National University-Ho Chi Minh City, 268 Ly Thuong Kiet, Dien Hong, Ho Chi Minh City, 70000, Vietnam*

based MOFs exhibit superior thermal stability, smoke-suppressing capability, and potential catalytic activity for promoting char formation.[33] However, pristine MOFs usually provide limited flame-retardant efficiency, and their interfacial compatibility with the polymer matrix requires further enhancement due to their tendency to agglomerate.[34] To address these challenges, modification of MOFs has proven to be an effective approach. For instance, di(*para*-aminobenzoic acid)-containing Co-based metal–organic framework (P-MOF) was synthesized and incorporated into EP.[35] It was found that the total heat release (THR) and peak heat release rate (PHRR) of EP declined by 18.6% and 28%, respectively, with 2 wt% loading of P-MOF. Additionally, various flame retardants such, as layered double hydroxide,[36] α-zirconium phosphate,[37] silica,[38] graphene oxide,[39] diatomite,[40] dimethyl methylphosphonate,[41] ferrocene,[42] polyphosphazence,[43] have been successfully integrated with MOFs to enhance their fire resistance performance.

9,10-Dihydro-9-oxa-10-phosphaphenanthrene-10-oxide (DOPO) is a well-known reactive flame retardant featuring high thermal stability, strong radical-trapping ability, and efficient char-promoting characteristics.[44] Covalent or coordination incorporation of DOPO moieties into MOF structures can simultaneously introduce gas-phase quenching ability and condensed-phase catalytic activity, resulting in improved flame-retardant efficiency. Furthermore, the integration of such DOPO-modified MOFs with traditional IFR systems is expected to produce a dual-mode synergistic effect, enhancing both the char strength and the radical quenching performance.

In this work, an amino-functionalized metal–organic framework, Fe-MOF-NH_2 was chemically modified with DOPO through a nucleophilic substitution reaction, as illustrated in Fig. 1. Fe-MOF-NH_2 was first synthesized *via* a solvothermal method, followed by its chemical modification with chlorinated DOPO to introduce phosphorus-containing groups onto the framework (labeled as MOF-DOPO). Subsequently, MOF-DOPO was combined with urea–melamine–formaldehyde microencapsulated APP (APP@UMF) at different mass ratios in the epoxy matrix. The resulting nanocomposites were systematically evaluated for their flame retardancy, thermo-oxidative stability, and mechanical properties using UL-94 vertical burning test, limiting oxygen index, thermogravimetric analysis, tensile, and impact tests. Moreover, the synergistic flame-retardant effect between MOF-DOPO and APP@UMF was discussed in both the condensed and gas phases.

2. Experimental

2.1 Materials

Epoxy resin (EPICOTE™ Resin MGS LR 385, epoxy equivalent: 160–170 g per equivalent, epoxy value: 0.58–0.64 equivalent 100 g^{-1}, viscosity: 700–1050 mPas)[45] and hardener (EPICURE™ Curing Agent MGS LH 386, 3-aminomethyl-3,5,5-trimethylcyclohexylamine (35–50 wt%), trimethylolpropane poly(oxypropylene) triamine (25–35 wt%), 2,2′-dimethyl-4,4′-methylenebis(cyclohexylamine) (20–25 wt%), amine value: 480–550 mg KOH g^{-1}, viscosity: 40–90 mPas)[46] were provided by Hexion Specialty Chemicals (Germany). APP (form II, $n > 1000$) and DOPO (97%) were bought from Shanghai Macklin Biochemical Co., Ltd. (China). Iron(III) chloride hexahydrate ($FeCl_3 \cdot 6H_2O$, 97%), 2-aminoterephthalic acid (H_2BDC-NH_2, 98.5%), urea (≥ 98%), triethylamine (TEA, ≥ 99%, density: 0.728 g cm^{-3}) were purchased from Fisher Scientific (USA). Melamine (MEL, 99%), formaldehyde solution (37%), and *N*-chlorosuccinimide (NCS, 98%) were supplied by Sigma-Aldrich (USA). Analytical-grade NaOH, Na_2CO_3, H_2SO_4, *N*,*N*-dimethyl formamide (DMF), toluene, dichloromethane (DCM), and absolute ethanol were used as received without further purification.

2.2 Synthesis of Fe-MOF-NH_2

Fe-MOF-NH_2 was synthesized *via* a modified solvothermal procedure. Typically, $FeCl_3 \cdot 6H_2O$ (20 g) was dissolved in DMF (740 mL) under vigorous stirring to obtain a homogeneous solution. Then, H_2BDC-NH_2 (13.4 g) was added and stirred for 10 min, followed by the dropwise addition of NaOH solution (148 mL, 0.2 mol L^{-1}). After further stirring for 15 min, the reaction mixture was heated at 110 °C under reflux in an argon (or air) atmosphere for 20 h. The resulting precipitate was separated by centrifugation, washed several times with DMF and methanol, and then dried under vacuum at 120 °C for 12 h to obtain the dark-brown powder Fe-MOF-NH_2 of 14.65 g (under argon atmosphere). Details of characterization are provided in the SI. To ensure the formation of a pure MOF phase, Fe-MOF-NH_2 was synthesized under the inert atmosphere. In contrast, the sample prepared in air exhibited Fe_2O_3 impurities, as confirmed by XRD and SEM analyses (Fig. S1 and S2).

2.3 Chemical grafting of DOPO onto Fe-MOF-NH_2

2.3.1. Synthesis of DOPO-Cl. *N*-Chlorosuccinimide (1.48 g) was dissolved in toluene (30 mL), followed by the slow addition of DOPO (2.0 g) under continuous stirring. The reaction mixture was then stirred overnight at 50 °C. After completion, the insoluble by-products were removed by filtration, and the filtrate was concentrated using rotary evaporation to obtain a pale-yellow gel-like product (2.23 g, yield ∼96%), designated as DOPO-Cl. ^1H NMR (600 MHz, $CDCl_3$) δ 8.07 (dd, $J = 16.2$, 7.2 Hz, 1H), 8.0–7.94 (m, 2H), 7.78 (m, 1H), 7.57 (m, 1H), 7.45 (t, $J = 7.8$ Hz, 1H), 7.36 (m, 1H), 7.30–7.27 (m, 1H). ^{31}P NMR (243 MHz, $CDCl_3$) δ 20.0 (Fig. S3).

2.3.2. Synthesis of MOF-DOPO. MOF-DOPO was prepared *via* a nucleophilic substitution reaction between Fe-MOF-NH_2 and DOPO-Cl. Briefly, DOPO-Cl (2.23 g) was dissolved in DCM (20 mL) under an argon atmosphere. Meanwhile, Fe-MOF-NH_2 (10.0 g) was dispersed in DCM (70 mL), followed by the addition of TEA (3.76 mL) under continuous stirring for 10 min. Subsequently, the DOPO-Cl solution was added dropwise to the suspension. After the addition was complete, the reaction mixture was further stirred for 24 h at room temperature under an argon environment. The resulting solid was collected by filtration, washed three times with DCM, and dried in a vacuum oven at 80 °C for 12 h to obtain the MOF-DOPO powder.

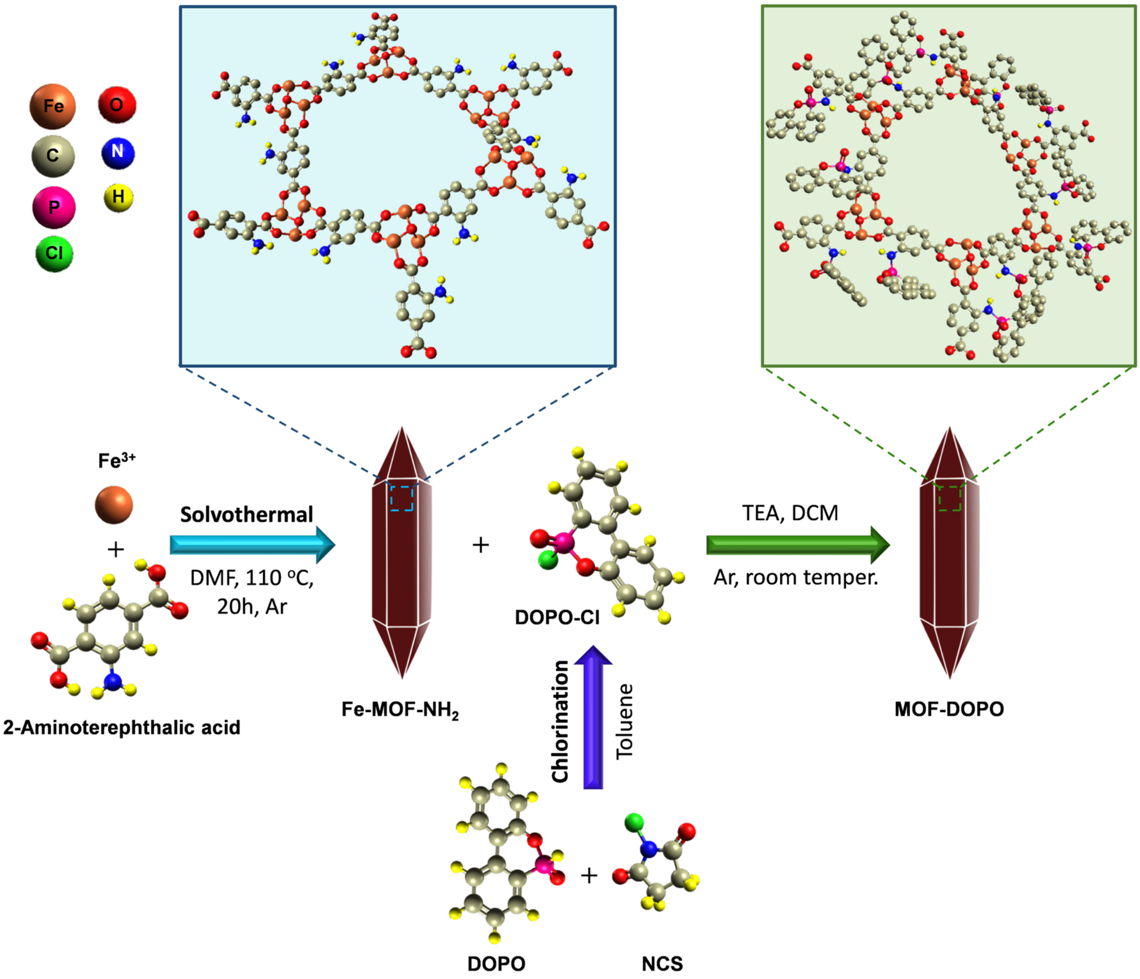

Fig. 1 Schematic presentation of synthesis route for MOF-DOPO.

2.4 Preparation of APP@UMF

Ammonium polyphosphate was microencapsulated with a urea–melamine–formaldehyde (UMF) resin shell to obtain APP@UMF, following a previously reported procedure.[25] The detailed preparation steps and corresponding characterization are presented in the SI. The results of FT-IR, XRD, and SEM proved the successful preparation of APP@UMF (Fig. S4 and S5).

2.5 Preparation of epoxy nanocomposites

Epoxy nanocomposites were prepared using a curing process with an epoxy resin-to-hardener mass ratio of 100 : 34. MOF-DOPO was first dispersed into the epoxy resin, while APP@UMF was incorporated into the hardener using mechanical stirring and ultrasonication to ensure uniform dispersion. The two mixtures were subsequently combined under gentle stirring to obtain a homogeneous blend, which was then poured into silicone molds of standard dimensions. The curing process was carried out at room temperature for 24 h, followed by post-curing at 60 °C for 12 h. The detailed formulations of the epoxy composites are listed in Table 2.

2.6 Characterizations

Fourier transform infrared (FT-IR, L1600400, PerkinElmer, USA) spectroscopy was used to identify functional groups in the samples *via* the KBr pellet technique. The FT-IR spectra were recorded over the wavenumber range from 400 to 4000 cm^{-1} at a resolution of 1 cm^{-1}. The crystalline structures of the materials were determined by X-ray diffraction (XRD, D8 Advance, Bruker, Germany) using Cu Kα radiation ($\lambda = 1.5406$ Å) within a 2θ range of 5–70°. The morphology of the samples was observed using field-emission scanning electron microscopy (FE-SEM, JSM-IT800, JEOL, Japan) operated at an accelerating voltage of 3 kV. Before observation, the samples were sputter-coated with a thin platinum layer using a JEC-3000FC coater (JEOL, Japan) for 60 s to improve conductivity. The elemental composition and distribution of C, O, Fe, N, and P in MOF-DOPO were analyzed by energy-dispersive X-ray spectroscopy (EDS mapping) on the JSM-IT800 microscope equipped with an Ultim Max 65 detector (Oxford Instruments, Japan). The successful synthesis of DOPO-Cl was demonstrated by ^1H and ^{31}P NMR spectra on a 600 MHz AvanceNEO spectrometer (Bruker) with $CDCl_3$ as a solvent. Thermogravimetric analysis (TGA, LABSYS Evo STA, Setaram, France) was performed to evaluate the thermal properties of Fe-MOF-NH_2, MOF-DOPO, and epoxy composites. The measurements were conducted in a temperature range of 50 to 900 °C at a heating rate of 10 °C min^{-1} under either air or nitrogen atmosphere.

The UL-94 vertical burning (UL94-V) test was conducted following ASTM D3801 using a GT-MC35F-2 instrument (Gester, China). Limiting oxygen index (LOI) values were determined based on ASTM D2863-13 using a Yasuda 214 oxygen index tester (Japan). For both tests, the epoxy composite specimens had dimensions of 125 mm × 13 mm × 3.2 mm.

The mechanical behavior of epoxy composites was characterized through tensile and impact measurements. Tensile properties were determined on a universal testing machine (AI-7000M, Gotech, Taiwan) in accordance with ISO 527 at a loading rate of 20 mm min^{-1}. The dog-bone specimens had a gauge length of 50 mm. Impact resistance was examined by the unnotched Izod method in accordance with ASTM D4812 on a mechanical testing system (TestResources, USA), employing samples with dimensions of 64 mm × 13 mm × 3 mm. All reported values represent the average of five independent measurements, and the corresponding standard deviations were included as error values.

3. Results and discussion

3.1 Characterization of MOF-DOPO

FT-IR analysis was performed to investigate the chemical structures of Fe-MOF-NH_2, MOF-DOPO, and DOPO (Fig. 2a and b). Both FT-IR spectra of Fe-MOF-NH_2 and MOF-DOPO display the characteristic bands of the Fe-MOF-NH_2 framework at 3462 and 3356 cm^{-1} (N–H vibrations), 1336 and 1257 cm^{-1} (C–N vibrations in aromatic amines), 1575–1384 cm^{-1} (carboxylate groups), and 520–579 cm^{-1} (Fe–O stretching modes).[47–49] Additionally, the FT-IR spectrum of MOF-DOPO exhibits a new peak at 1145 cm^{-1}, corresponding to P–O–Ar vibrations of DOPO.[50] The absorption peaks at 766 and 620 cm^{-1} become broader and more intense due to the overlap of vibrations in MOF and DOPO, with the 766 cm^{-1} band arising from Ar–C–H.

(MOF) and P–O–Ar (DOPO) vibrations,[50,51] and the 620 cm^{-1} band attributed to Fe–O (MOF) and P=O (DOPO) vibrations.[52,53] In particular, the appearance of new absorption peaks at around 1093 and 915 cm^{-1}, assigned to P–N vibrations,[54,55] demonstrates the formation of covalent linkages between DOPO and Fe-MOF-NH_2. In addition, the disappearance of P–H stretching bands at 2435 and 2384 cm^{-1} indicates that DOPO no longer exists in the free molecular state in the MOF-DOPO sample.

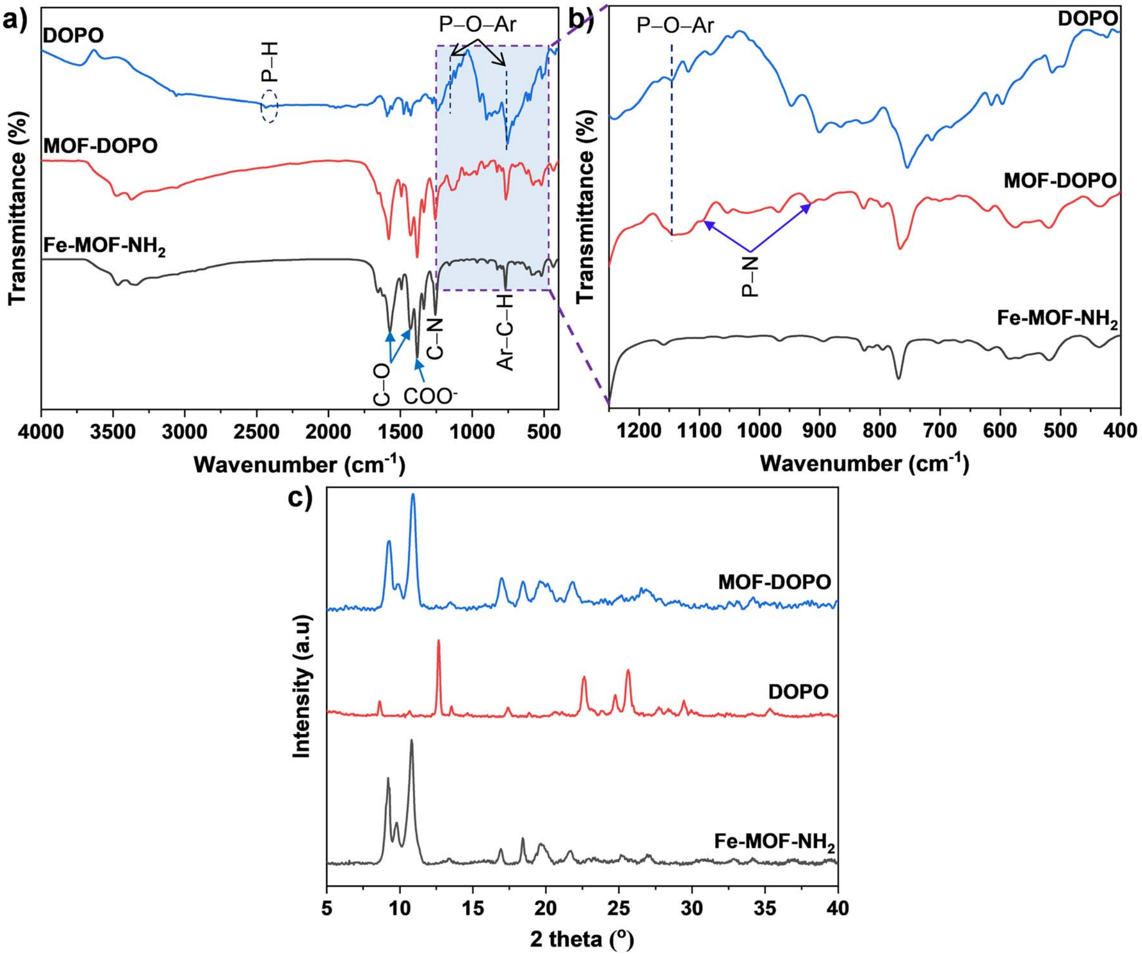

Fig. 2 FT-IR spectra (a), magnified FT-IR spectra (b) and XRD patterns (c) of Fe-MOF-NH_2, MOF-DOPO, and DOPO.

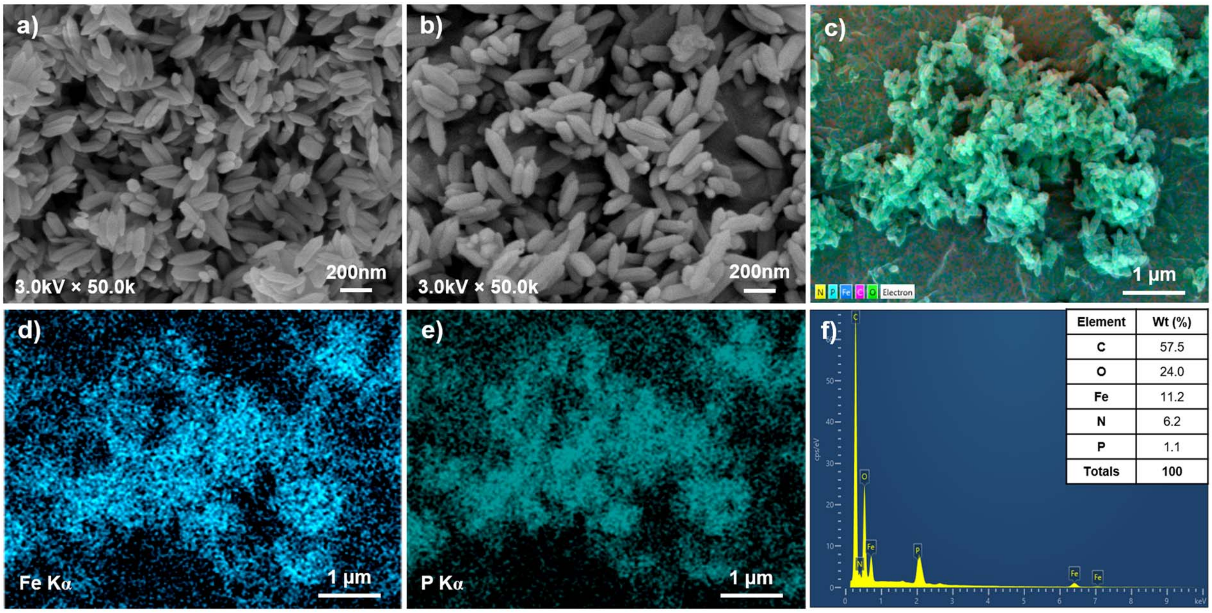

Element	Wt (%)
C	57.5
O	24.0
Fe	11.2
N	6.2
P	1.1
Totals	100

Fig. 3 SEM images of Fe-MOF-NH_2 (a), MOF-DOPO (b), EDS mapping of MOF-DOPO (c), Fe (d), and P (e) elements in MOF-DOPO, and EDS spectrum of MOF-DOPO (f).

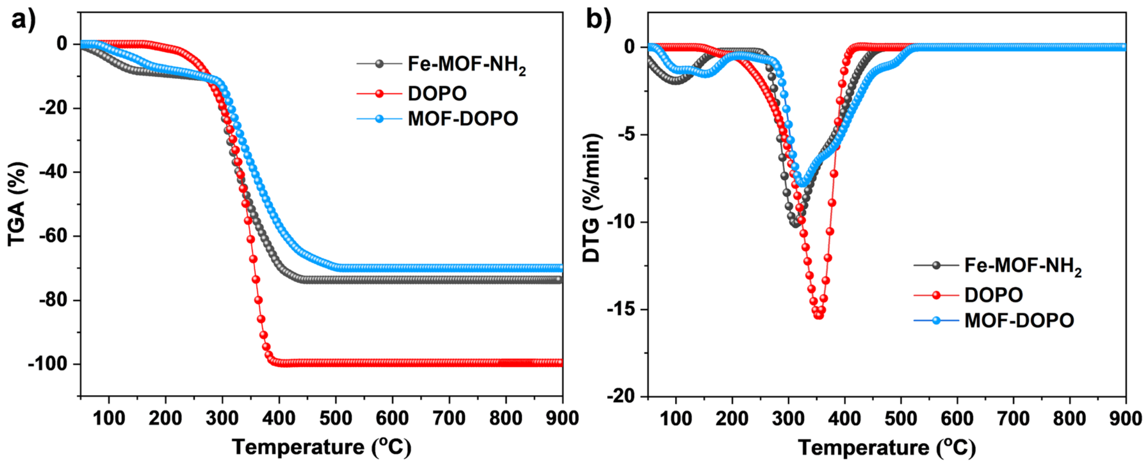

Fig. 4 TGA (a) and DTG (b) curves of Fe-MOF-NH_2, DOPO, and MOF-DOPO in N_2 atmosphere.

These results confirm the successful chemical grafting of DOPO to the Fe-MOF-NH_2 framework.

The crystalline structure of the samples was analyzed by X-ray diffraction (Fig. 2c). The XRD pattern of MOF-DOPO exhibits the same diffraction reflections as pristine Fe-MOF-NH_2, indicating that the crystalline framework of Fe-MOF-NH_2 is preserved after modification. Moreover, no characteristic diffraction peaks assignable to DOPO are observed, suggesting that DOPO does not exist as a free crystalline phase. Instead, it is covalently grafted to the Fe-MOF-NH_2 framework, which does not exhibit long-range crystalline order detectable by XRD.

As shown in Fig. 3a, the as-synthesized Fe-MOF-NH_2 exhibits hexagonal spindle-shaped crystals with a length ranging from 150 to 235 nm and an average diameter of approximately 60 nm. After modification, the morphology of MOF-DOPO (Fig. 3b) remains essentially unchanged compared with the pristine Fe-MOF-NH_2. This observation further corroborates the XRD results, confirming that the structural integrity of Fe-MOF-NH_2 is well preserved after DOPO grafting. The successful grafting of DOPO to Fe-MOF-NH_2 framework was further verified by EDS spectroscopy. The overlay image (Fig. 3c) reveals the presence of all constituent elements of the MOF and DOPO (C, O, N, Fe, and P), which are uniformly distributed throughout the crystallites, indicating a homogeneous composition without visible phase separation. In particular, the Fe and P elemental maps (Fig. 3d and e) display highly similar spatial distributions, with signals spreading consistently over the spindle-shaped structures. The uniform dispersion of phosphorus strongly suggests that DOPO is grafted onto Fe-MOF-NH_2 framework rather than aggregated as a separate crystalline phase. Additionally, Fig. 3f presents the

Table 1 TGA parameters of Fe-MOF-NH_2, DOPO, and MOF-DOPO in N_2 atmosphere

Samples	$T_{5\%}$[a] (°C)	T_{max}[b] (°C)	Residue at 900 °C (wt%)
Fe-MOF-NH_2	104.48	312.71	26.29
DOPO	250.8	353.4	0.4
MOF-DOPO	152.18	324.63	29.99

[a] $T_{5\%}$: temperature at mass loss of 5 wt%. [b] T_{max}: temperature at maximum degradation rate.

EDS spectrum of MOF-DOPO along with the corresponding elemental mass proportions. The phosphorus content was determined to be 1.1 wt%, which corresponds to a DOPO content of about 7.66 wt% in the MOF-DOPO sample, as calculated using eqn (1).

$$\mathrm{DOPO(wt\%)} = \frac{P(\mathrm{wt\%})}{w_{\mathrm{P}}} \times 100 \tag{1}$$

where, P (wt%) is mass percentage of P element determined from EDS analysis w_{P} is the mass fraction of phosphorus in DOPO (14.34 wt%).

Thermal behavior of Fe-MOF-NH_2, DOPO, and MOF-DOPO were investigated by thermogravimetric analysis under a N_2 atmosphere, TGA and derivative thermogravimetry (DTG) curves are displayed in Fig. 4. Additionally, the characteristic parameters, including temperatures at the mass loss of 5 wt% ($T_{5\%}$), temperatures at maximum mass loss rate (T_{max}), and the char residue at 900 °C, are summarized in Table 1. For Fe-MOF-NH_2, the first mass loss at a temperature observed below 250 °C corresponds to the volatilization of physically adsorbed molecules on the surface and within the pores of the framework. The second mass loss, occurring between 285 and 470 °C with a maximum mass loss at 312.71 °C, is attributed to the decomposition of the organic skeleton.[48] In the case of DOPO, decomposition takes place between 250 and 400 °C, leaving only a negligible char residue of 0.4%. The thermal degradation profiles of Fe-MOF-NH_2 and MOF-DOPO are similar, showing two major mass loss steps. However, compared with Fe-MOF-NH_2, both the $T_{5\%}$ and T_{max} values of MOF-DOPO notably increase by around 47.7 °C and 11.92 °C, respectively, indicating an enhancement in thermal stability after grafting DOPO. Moreover, the residual char of MOF-DOPO (29.99%) is higher than that of Fe-MOF-NH_2 (26.29%) as well as the calculated residue (24.3%- estimated based on the individual TGA residues of Fe-MOF-NH_2 (26.29%) and DOPO (0.4%), assuming a DOPO grafting content of 7.66% as determined by EDS). These results suggest a synergistic interaction between DOPO and the

Table 2 Formulation of epoxy composites and their flame retardancy[a]

	Compositions (wt%)				UL-94 test (3.2 mm)			
Samples	EP	APP@UMF	Fe-MOF-NH_2	MOF-DOPO	Rating	t_1[b] (s)	t_2[c] (s)	LOI (%)
EP0	100				NR	Burnt out	—	21.1
EP1	90	10			V-0	1.2	1.5	28.5
EP2	90	9	1		V-0	0.9	1.3	30.7
EP3	90	9		1	V-0	0.5	0.6	37.3
EP4	90	7		3	V-0	0.8	1.0	33.8
EP5	90	5		5	V-1	10.3	2.6	24.6

[a] Abbreviation NR: No rating. [b] t_1: Self-extinguishing time after the first ignition. [c] t_2: Self-extinguishing time after the second ignition.

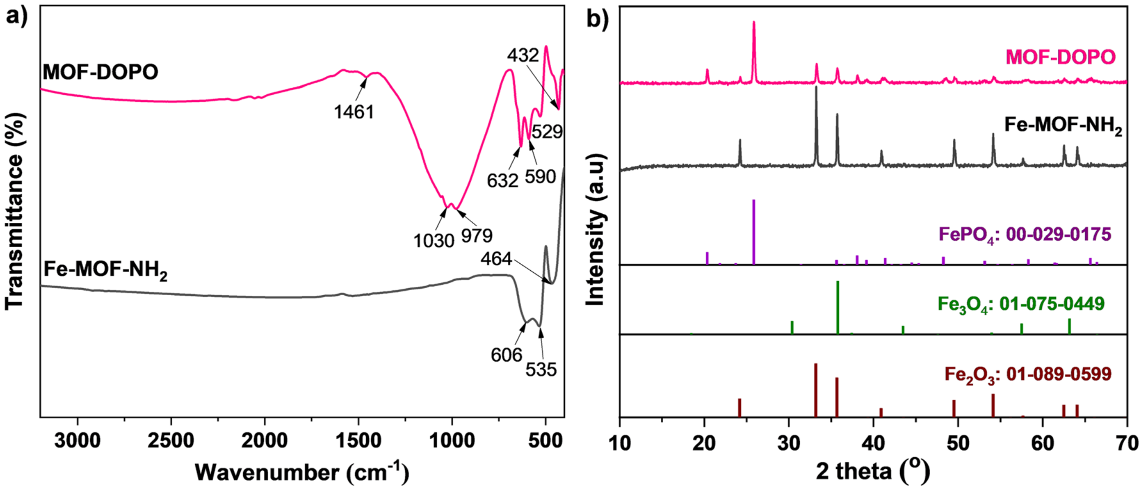

Fig. 5 FT-IR spectra (a) and XRD patterns (b) of Fe-MOF-NH_2 and MOF-DOPO after calcination at 900 °C in N_2 atmosphere.

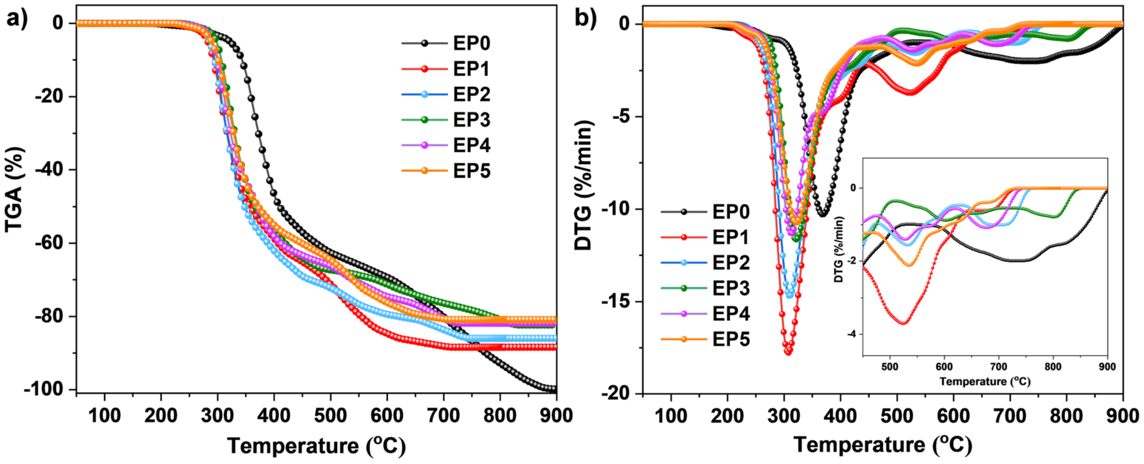

Fig. 6 TGA (a) and DTG (b) curves of epoxy and its composites in air atmosphere.

MOF framework in improving the thermal stability and char-forming capability of MOF-DOPO.

To elucidate this phenomenon, the residues of Fe-MOF-NH_2 and MOF-DOPO after calcination at 900 °C under N_2 atmosphere were characterized by FT-IR and XRD (Fig. 5). The FT-IR spectra of both residues (Fig. 5a) exhibit characteristic bands of iron oxides at 430–460 cm^{-1} (Fe–O vibrations in the octahedral sites of Fe_2O_3), 520–530 cm^{-1} (Fe–O vibrations in the tetrahedral sites of Fe_2O_3), and 570–610 cm^{-1} (Fe–O vibrations in Fe_3O_4).[56,57] In addition, the residue of MOF-DOPO shows new peaks at 1030 and 979 cm^{-1} (PO_4 vibrations) and 632 cm^{-1} (P–O vibrations), suggesting the formation of phosphate species.[58,59] The XRD pattern of the MOF residue confirms the formation of Fe_2O_3, with diffraction peaks at 2θ ~24.19°, 33.14°, 35.70°, 40.92°, 49.48°, 54.15°, 62.46°, and 64.01° (ICDD PDF # 01-089-0599), along with a minor amount of Fe_3O_4 at 2θ ~35.70° and 57.69° (ICDD PDF # 01-075-0449). Meanwhile, the XRD pattern of the MOF-DOPO residue reveals not only the presence of iron oxides but also additional reflections at 2θ ~20.3°, 25.9°, 38.08°, 48.38°, and 65.73°, which can be assigned to iron phosphate ($FePO_4$) (ICDD PDF # 00-029-0175). These observations are in good agreement with the FT-IR results. The formation of $FePO_4$ can be attributed to the chemical reaction between iron oxides and phosphoric acid species generated during the thermal decomposition of MOF-DOPO.

Table 3 TGA parameters of epoxy and its composites in air atmosphere

Samples	$T_{5\%}$[a] (°C)	T_{max}[b] (°C) 1	2	3	Residue at 900 °C (wt%)
EP0	317.54	368.31	718.45	—	0.12
EP1	283.25	307.2	527.34	—	11.58
EP2	286.12	309.50	534.35	699.20	14.04
EP3	298.21	321.45	597.25	804.06	17.68
EP4	290.11	313.00	528.29	683.92	18.17
EP5	289.79	321.56	535.55	—	19.15

[a] $T_{5\%}$: temperature at mass loss of 5 wt%. [b] T_{max}: temperature at maximum degradation rate.

3.2 Thermo-oxidative property

The thermo-oxidative behavior of epoxy and its composites was evaluated *via* thermogravimetric analysis in air, and corresponding TGA and DTG curves are depicted in Fig. 6. Important TGA parameters, including $T_{5\%}$ (temperatures at mass loss of 5 wt%), T_{max} (temperatures at maximum decomposition rate), and residue at 900 °C, are summarized in Table 3. Compared with EP0, the EP1 composite exhibits lower $T_{5\%}$, T_{max1}, and T_{max2} values.

The reduction in $T_{5\%}$ can be associated with the inferior thermal stability of the UMF resin shell in APP@UMF. Upon decomposition, UMF resin releases nonflammable gases (NH_3, CO_2), which act as blowing agents to facilitate the development of an intumescent char structure.[25] Meanwhile, the decline in the T_{max} values results from the catalytic effect of phosphoric acid and its derivatives formed from the decomposition of APP, which accelerates early polymer degradation and promotes char formation,[60] thereby notably improving the flame retardancy of the epoxy matrix. This char-forming effect is corroborated by the substantial increase in char residue for EP1 (11.58%) compared to EP0 (0.12%). Compared to EP1, the nanocomposites exhibit higher thermo-oxidative stability, as evidenced by the pronounced increase in T_{max} values and char yield. This enhancement can be attributed to the catalytic effect of metal sites on carbonization,[30] contributing to the formation of a more stable char layer. Furthermore, the chemical interaction between the decomposition products of the flame-retardant additives (iron oxides and phosphoric species) can generate thermally stable phosphate compounds, reinforcing the char layer, thereby slowing down the oxidative degradation of the char layer. Among all nanocomposites, the EP3 nanocomposite demonstrates superior thermal oxidative stability, with T_{max2} and T_{max3} significantly shifted to 597.25 and 804.06 °C, respectively. Moreover, the char yield of EP3 (17.68%) surpasses compared to EP2 (14.04%), indicating that DOPO grafting onto Fe-MOF-NH_2 notonly enhances thermal stability but also promotes char formation. These results provide a partial explanation for the outstanding fire resistance of the nanocomposite containing 1 wt% MOF-DOPO and 9 wt% APP@UMF. The residual char further increases with higher MOF-DOPO loading (EP4 and EP5), which can be attributed to the generation of a greater quantity of high-molecular-weight metal phosphates.

3.3 Flame resistance

The flame retardancy of epoxy resin and its composites was investigated through the UL94-V and LOI tests, and results are presented in Table 2. Neat epoxy (EP0) exhibits high flammability, as evidenced by its low LOI value of 21.1% and complete combustion immediately after the first ignition. Incorporation of 10 wt% APP@UMF markedly improves the flame retardancy of epoxy. In particular, the EP1 composite achieves a UL-94 V-0 rating, along with a notable increase in LOI to 28.5%. Besides, the synergistic flame-retardant effect between APP@UMF and Fe-MOF-NH_2 or MOF-DOPO was also investigated while maintaining a constant total additive content of 10 wt%. Compared to the EP1 composite, the combination of APP@UMF and Fe-MOF-NH_2 or MOF-DOPO leads to a pronounced enhancement in the flame retardant efficiency of the epoxy resin. Notably, the MOF-DOPO material demonstrates a superior synergistic flame-retardant effect. This result demonstrates the crucial role of DOPO functionalization in enhancing the synergistic flame-retardant efficiency of MOF with APP@UMF. The optimal ratio between MOF-DOPO and APP@UMF was also studied by UL-94 and LOI tests. The results reveal that the EP3 nanocomposite, containing 1 wt% MOF-DOPO and 9 wt% APP@UMF, exhibits the highest fire resistance among all nanocomposites. Specifically, EP3 achieves a UL-94 V-0 rating with the shortest self-extinguishing times ($t_1 = 0.5$ s and $t_2 = 0.6$ s) and an outstanding LOI value of 37.3%. The remarkable increase in LOI of EP3 highlights a significant synergistic effect between MOF-DOPO and APP@UMF, demonstrating that even a small addition of MOF-DOPO can substantially enhance the flame-retardant performance of epoxy composites. However, the flame retardant efficiency of nanocomposites tends to decrease with increasing MOF-DOPO content. Notably, the EP5 nanocomposite, loading 5 wt% MOF-DOPO and 5 wt% APP@UMF, attains only a UL-94 V-1 rating accompanied by a substantial reduction in LOI to 24.6%, which is even lower than that of EP1. These results indicate that optimization of the MOF-DOPO to APP@UMF ratio is critical for achieving maximum synergistic flame-retardant efficiency in epoxy nanocomposites.

3.4 Morphology of char residue

To investigate the synergistic flame retardant effect between MOF-DOPO and APP@UMF in the epoxy matrix, equal-mass composite samples were calcined at 900 °C with a heating rate of 10 °C min^{-1} in air. The resulting residual chars were

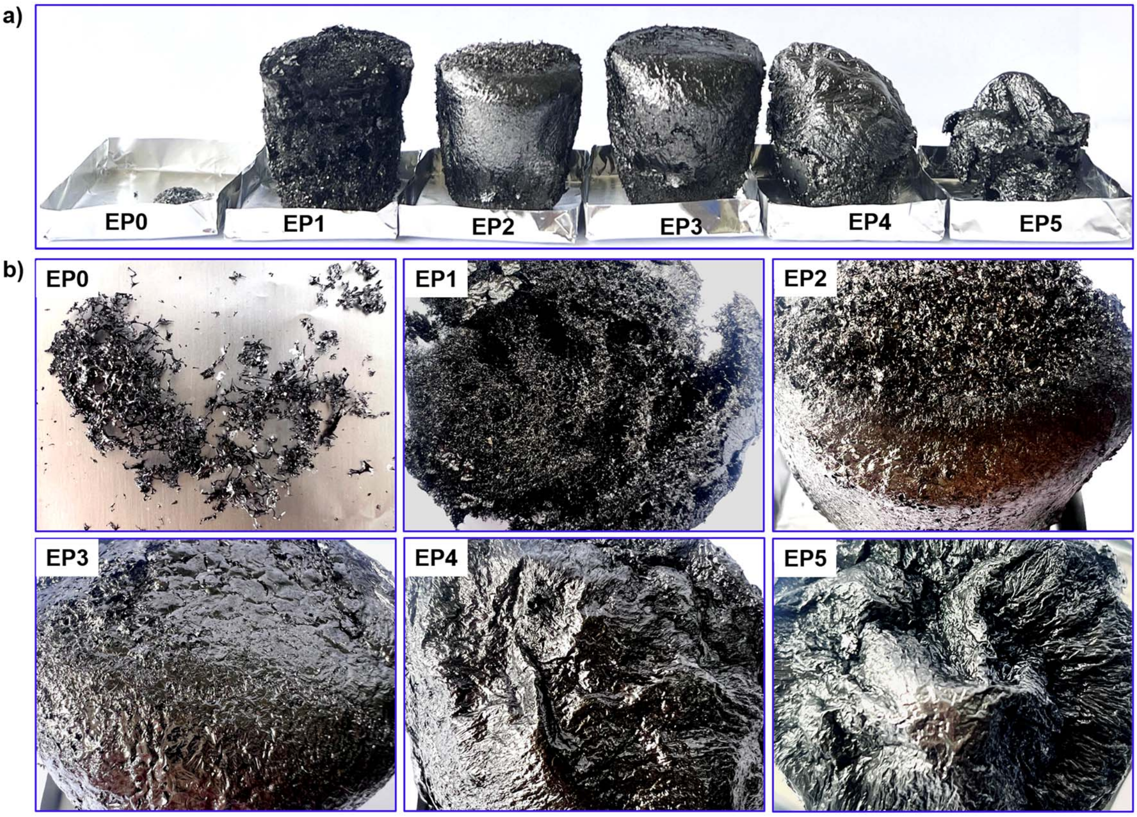

Fig. 7 Digital photographs of EP and its composites obtained after calcination at 900 °C: Side view (a) and Top view (b).

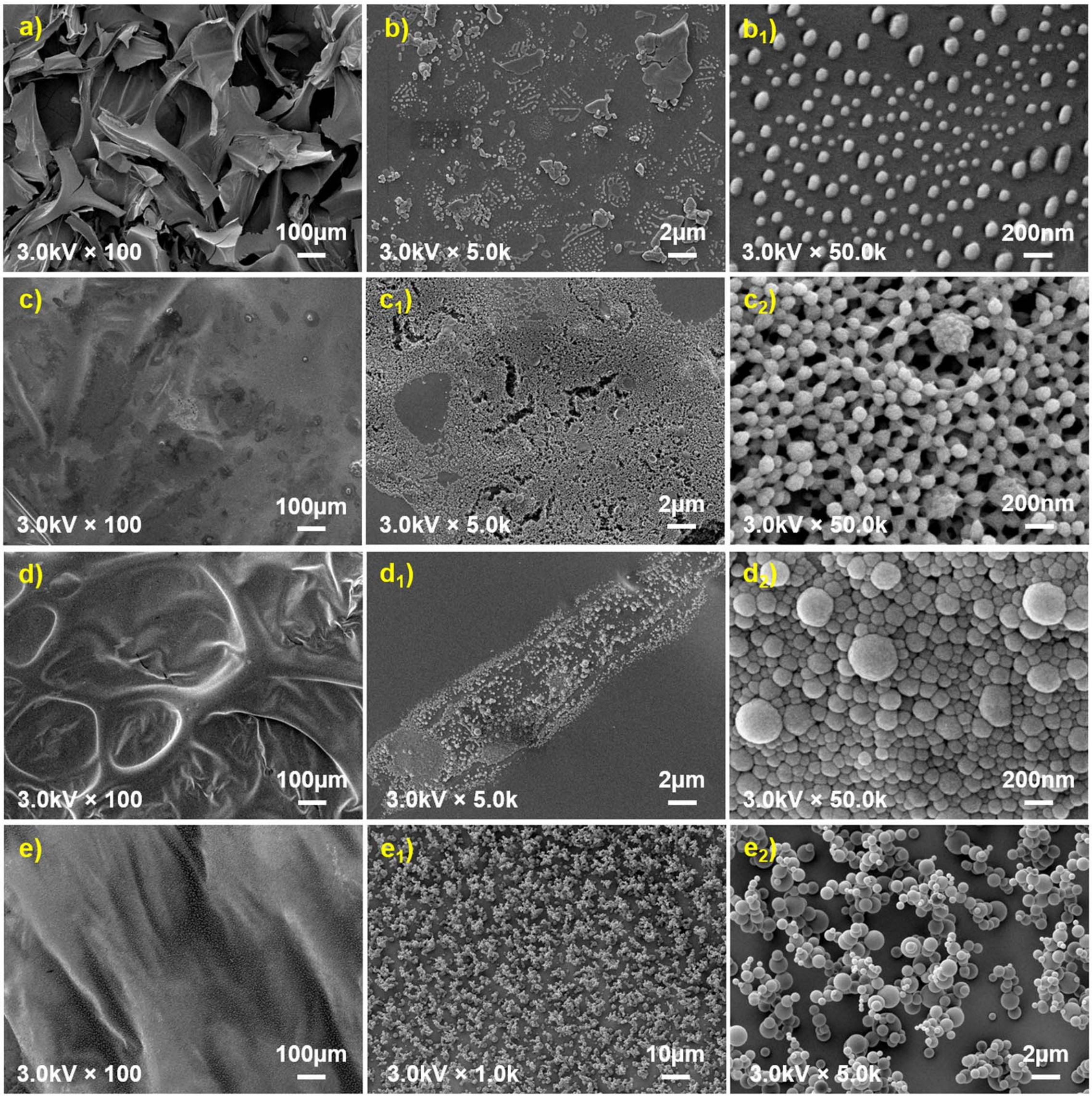

Fig. 8 The surface morphology of EP1 (a), EP2 (b and b_1), EP3 (c, c_1 and c_2), EP4 (d, d_1 and d_2), EP5 (e, e_1 and e_2) after calcination at 900 °C.

then characterized by SEM, FT-IR, and XRD. Fig. 7 shows the digital photographs of the char layer obtained after calcination. The EP0 sample leaves a negligible amount of residual char, in agreement with the TGA results. In contrast, the introduction of flame-retardant additives greatly enhances the char formation. The EP1 composite generates a voluminous intumescent char layer; however, its structure is relatively porous, soft, and mechanically weak, making it prone to collapse. With the incorporation of 1 wt% Fe-MOF-NH_2, the char structure of EP2 becomes denser and mechanically stronger. Compared to EP2, the EP3 nanocomposite exhibits a more voluminous char layer, demonstrating that DOPO further facilitates carbonization. Moreover, the continuity and compactness of the char layer surface of EP3 are clearly improved, suggesting the stronger stronger reinforcing effect of MOF-DOPO compared to Fe-MOF-NH_2. At higher MOF-DOPO loadings, the char structures of the nanocomposites become increasingly rigid and robust, but their intumescence is substantially diminished, particularly in the case of EP5.

Fig. 8 illustrates the SEM micrographs of the char layer surfaces. In the case of EP1 (Fig. 8a), the char layer reveals a fragmented and of loosely packed structure composed of thin and brittle carbonaceous flakes, resulting in a fragile and porous structure. Although this intumescent char layer can act as a barrier to heat and oxygen diffusion, thereby offering some degree of thermal protection, its weak structural integrity renders it susceptible to collapse under elevated temperatures or vigorous airflow. Consequently, the overall protective capability of this layer remains insufficient without further reinforcement. Conversely, the char surfaces of the nanocomposites (EP2–EP5) show a more compact and continuous morphology (Fig. 8b–e), reflecting improved structural integrity. Notably, a network of spherical particles covering the char structures can be observed, evidencing the formation of multicomponent char

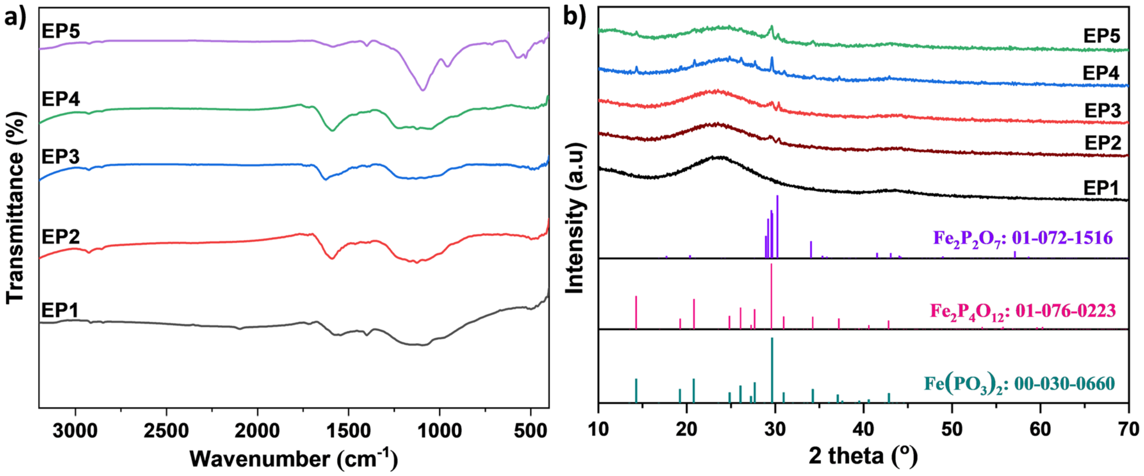

Fig. 9 FT-IR spectra (a) and XRD patterns (b) of epoxy composites EP1–EP5 after calcination at 900 °C.

structures. The particle size progressively increases with higher nanoparticle loadings, ranging from approximately 100 nm at 1 wt% Fe-MOF-NH_2 (Fig. 8b_1) or MOF-DOPO (Fig. 8c_2) to several hundred nanometers at 3 wt% MOF-DOPO (Fig. 8d_2), and reaching nearly 1 μm at 5 wt% MOF-DOPO (Fig. 8e_2). These spherical entities play a crucial role in reinforcing the char framework and enhancing its thermal stability. Furthermore, the development of this thermally stable particulate network may exert a "lotus-leaf effect", impeding direct flame contact with the underlying material and thereby improving the protective capability of the char layer.

3.5 Flame-retardant mechanism

Fig. 9 presents FT-IR spectra and XRD patterns of the char residues. As observed in Fig. 9a, the char residue of EP1 displays absorption bands at 2925–2854 (–CH_2 stretching), 1724 (C=O stretching), 1536–1636 (C=C stretching in aromatic ring), and 1400 cm^{-1} (C–C stretching in aromatic ring),[61–66] indicating that aromatization, esterification, and carbonization processes take place during the thermal decomposition of the epoxy composite. Additionally, characteristic peaks at 1168 (P=O stretching), 1096–975 (P–O–C linkage), and 500 cm^{-1} (O=P–O bonding)[10,66–68] confirm the formation of the phosphorus-rich char layer. For EP2–EP4, apart from the absorption peaks similar to those of EP1, new weak absorption bands appear at 550–600 and 430–460 cm^{-1}, attributed to O–P–O bending and Fe–O vibrations in metal phosphate compounds.[65,69] These features verify the generation of metal-phosphate compounds within the char structures. Moreover, additional bands detected at 714–747 cm^{-1} correspond to P–N–C bonding,[70] implying that the P–N–C char structure of the nanocomposites is formed and effectively stabilized at elevated temperatures owing to the presence of thermally stable metal phosphates. In the case of EP5, noticeable changes are observed compared to EP2–EP4. Specifically, the peak intensity associated with the aromatic carbonaceous structure at about 1586 cm^{-1} (C=C in aromatic ring) significantly diminishes, whereas the signals corresponding to metal phosphates at 1093, 957, and 572–528 cm^{-1} become sharper and more intense. These observations indicate that metal phosphate species dominate the composition of the EP5 char structure.

As shown in Fig. 9b, the XRD pattern of EP1 residue exhibits no distinct diffraction peaks, suggesting that the char is predominantly amorphous in nature. Meanwhile, the broad peaks at $2\theta \sim 29.61°$ and 30.40° in the XRD patterns of EP2 and EP3 residues can be assigned to characteristic reflections of iron phosphate species, including iron metaphosphate ($Fe(PO_3)_2$, ICDD PDF # 00-030-0660), iron tetraphosphate ($Fe_2P_4O_{12}$, ICDD PDF # 01-076-0223), and iron pyrophosphate ($Fe_2P_2O_7$, ICDD PDF # 01-072-1516), with $Fe_2P_2O_7$ being the predominant phase. Other diffraction peaks of these phosphates may be obscured by the high background of the amorphous char. The findings reveal that the spherical particles covering the surface of the intumescent char layers are the mixture of the thermally stable phosphate compounds. As the MOF-DOPO content in the nanocomposite increases, the diffraction peaks of phosphate species in the char matrix become shaper and more intense. The spherical particles on the surface of EP_4 and EP_5 remain composed of multiple phosphate phases; however, $Fe_2P_4O_{12}$ and $Fe(PO_3)_2$ are predominant compared to $Fe_2P_2O_7$.

According to the above analyses of the morphology and composition of char residues, combined with previous reports, a plausible synergistic flame-retardant mechanism of APP@UMF and MOF-DOPO in the epoxy nanocomposite is illustrated in Fig. 10. Initially, the degradation of the UMF shell layer and amine curing agents releasing a large amount of nonflammable gases (NH_3, CO_2, and H_2O), which dilute the oxygen concentration and cool the combustion zone. Concurrently, the decomposition of DOPO moieties generates phosphorus-containing radicals ($HPO^{\bullet}$, $PO^{\bullet}$, and $PO_2^{\bullet}$) that effectively capture high-energy flame-propagating radicals ($H^{\bullet}$, $HO^{\bullet}$, and $O^{\bullet}$), thereby suppressing the gas-phase combustion reactions. Meanwhile, the pyrolysis of DOPO and APP produces phosphoric acid and its derivatives (pyro-, ultra-, and poly-phosphoric acids), which can catalyze the dehydration, esterification, and aromatization reactions of the epoxy matrix,

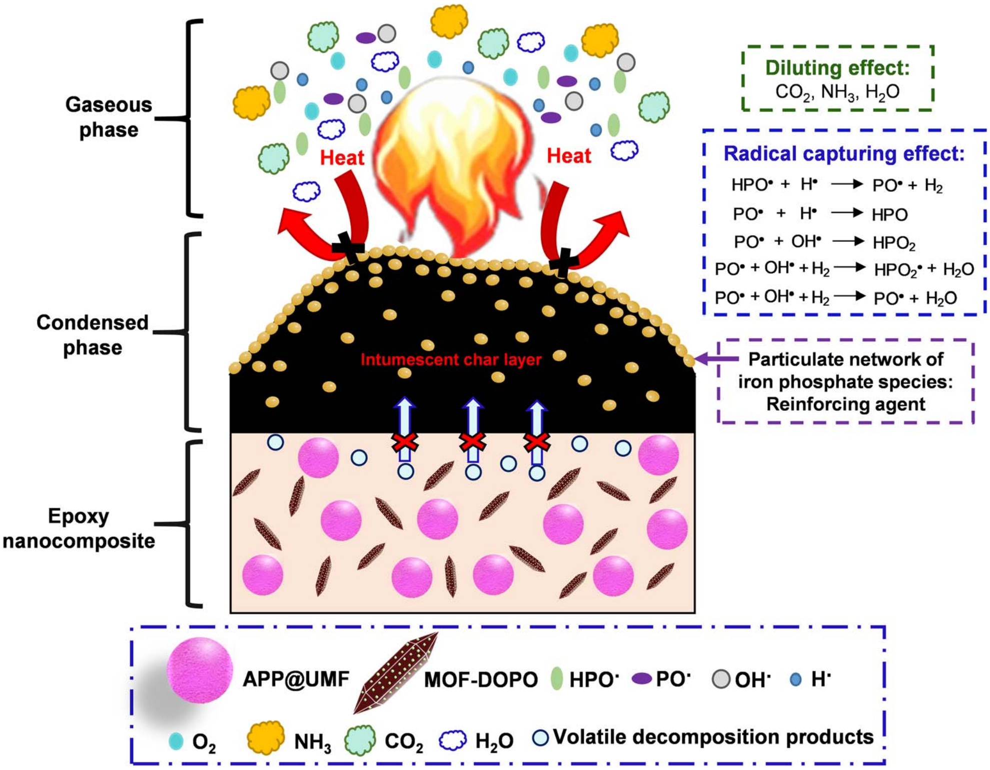

Fig. 10 Possible flame-retardant mechanism of epoxy nanocomposite containing APP@UMF and MOF-DOPO.

promoting the formation of a phosphorus-rich aromatic char layer. The evolved noncombustible gases simultaneously act as blowing agents, promoting the expansion and intumescence of this protective char layer. Acting as a thermal and mass transfer barrier, this carbonaceous layer insulates the underlying polymer and mitigates further degradation. Moreover, the phosphoric species react with iron oxides formed from decomposition of MOF to generate thermally stable iron phosphate compounds, such as $Fe_2P_2O_7$, $Fe_2P_4O_{12}$, and $Fe(PO_3)_2$. These inorganic species form a particulate network that covers the surface of the intumescent char layer, enhancing its compactness and continuity. The resulting iron phosphate network not only reinforces the mechanical strength of the intumescent char but also imparts a "lotus-leaf effect", limiting direct flame impingement on the substrate. Consequently, the condensed-phase flame retardancy of the nanocomposite is greatly enhanced.

The combination of 1 wt% MOF-DOPO and 9 wt% APP@UMF is identified as the optimal formulation for achieve a strong synergistic flame-retardant effect, endowing the EP3 nanocomposite with superior fire resistance. In contrast, a higher MOF-DOPO loadings (3–5 wt%) consumes excessive phosphoric species for the formation of metal phosphates, which hinders the development of the intumescent char structure (as observed in Fig. 7), leading to a decline in the overall flame retardancy efficiency.

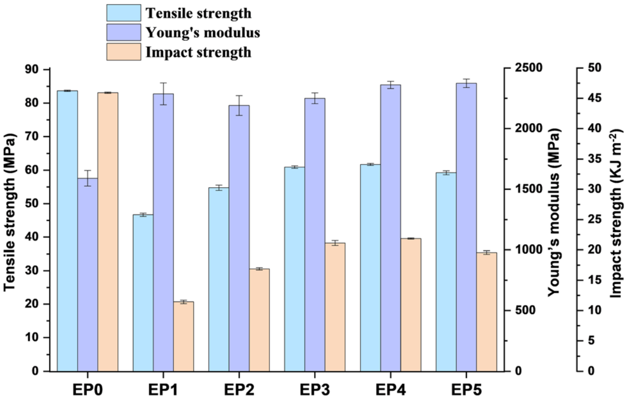

Fig. 11 The mechanical properties of EP and its composites.

3.6 Mechanical properties

The mechanical properties of epoxy and its composites were evaluated by tensile and unnotched Izod impact tests. The detailed parameters, including tensile strength, Young's modulus, and impact strength, are displayed in Fig. 11. For EP1, its Young's modulus increases owing to the presence of rigid inorganic filler; in contrast, tensile and impact strengths significantly reduce. Specifically, tensile and impact strengths of EP1 are 46.67 MPa and 11.43 KJ m^{-2}, which are much lower than those of EP0 by 44.23% and 75.11%, respectively. In general, the addition of APP@UMF negatively impacts the mechanical properties of the EP matrix. Although encapsulation with UMF resin enhances the compatibility of APP within the epoxy matrix, noticeable agglomeration of the

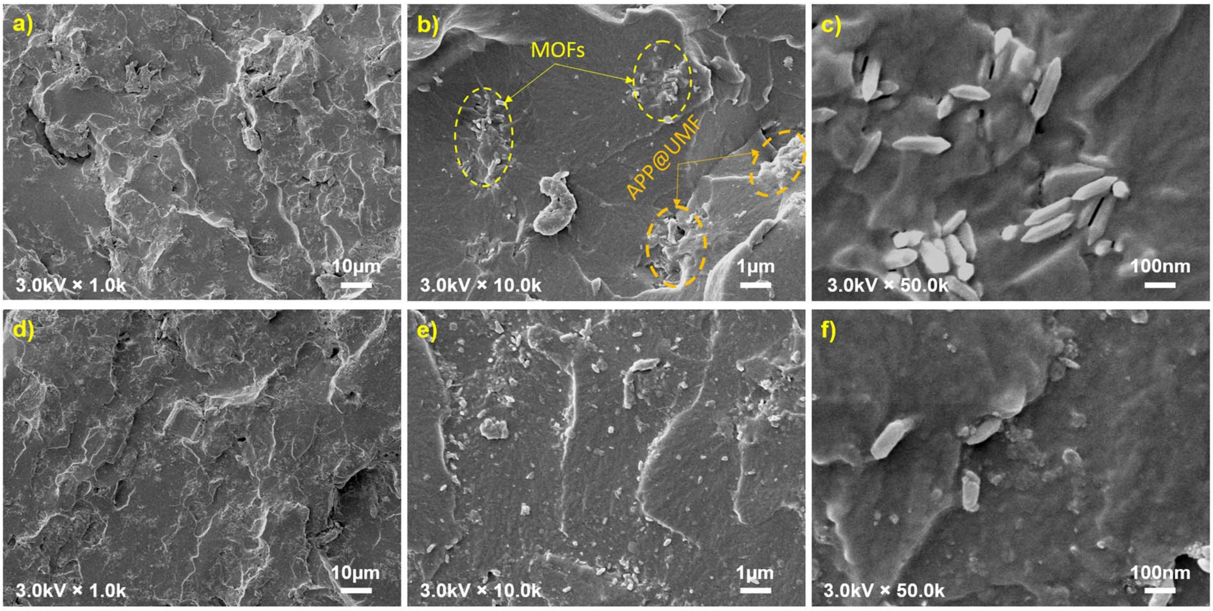

Fig. 12 The fracture surface of nanocomposites EP2 (a–c) and EP3 (d–f) at various magnifications.

microparticles can still be observed (Fig. 12a–e). Moreover, the relatively large particle size of this filler further compromises the mechanical performance of the composites, which hinders efficient stress transfer and induces brittleness in the polymer network. The partial substitution of APP@UMF with Fe-MOF-NH_2 or MOF-DOPO leads to an improvement in the mechanical properties of the APP@UMF/EP composite, and the reinforcing effect is more pronounced in the case of MOF-DOPO. Specifically, relative to EP1, the tensile and impact strengths of EP2 increase moderately by 17.33% and 47.78%, while those of EP3 exhibit substantial improvement of 30.6% and 84.78%, respectively. These results can be attributed to the slight agglomeration of unmodified Fe-MOF-NH_2 nanoparticles, as observed in Fig. 12b and c. In contrast, MOF-DOPO displays a more homogeneous distribution within the epoxy matrix (Fig. 12e and f). Among the nanocomposites loading varying MOF-DOPO contents, EP4 demonstrates the optimal balance, achieving tensile strength of 61.74 MPa and impact strength of 21.85 KJ m^{-2}. It is also noteworthy that the incorporation of MOF or MOF-DOPO has little influence on Young's modulus, which changes insignificantly compared to the EP1 composite. These findings suggest that MOF-DOPO not only enhances the flame retardancy but also reinforces the mechanical integrity of the epoxy composites, highlighting its potential for the development of high-performance flame-retardant nanocomposite materials.

4. Conclusions

In summary, Fe-MOF-NH_2 was successfully modified with DOPO through a chemical grafting method, yielding a grafting degree of 7.66 wt%. Subsequently, MOF-DOPO and APP@UMF were incorporated into the epoxy resin to prepare flame-retardant nanocomposites. The formulation containing 1 wt% MOF-DOPO and 9 wt% APP@UMF exhibited the most effective synergistic performance, achieving a high LOI value of 37.3% and a UL-94 V-0 rating. Thorough analyses of the char morphology and composition revealed that the flame-retardant synergism between MOF-DOPO and APP@UMF occurred in both gas and condensed phases. In the gas phase, the flame was inhibited due to the combined effects of radical quenching by DOPO-derived phosphorus radicals, as well as the dilution and cooling effects of the nonflammable gases released from the decomposition of MOF and APP@UMF. In the condensed phase, a phosphorus-rich intumescent char layer acts as a particulate network of thermally stable iron phosphate species ($Fe_2P_2O_7$, $Fe_2P_4O_{12}$, and $Fe(PO_3)_2$) not only enhanced the compactness and continuity of the char layer but also imparted a "lotus-leaf effect", effectively hindering direct flame contact with the underlying polymer matrix, thereby suppressing further effective insulating barrier. Moreover, the formation of the combustion. In addition, the presence of MOF-DOPO substantially alleviated the adverse impact of APP@UMF on the mechanical properties of the epoxy matrix. Therefore, the combination of MOF-DOPO and APP@UMF offers a promising strategy for manufacturing high-performance epoxy nanocomposites.

Author contributions

Conceptualization, Nhung Hac Thi, Mai Ha Hoang; methodology, Nhung Hac Thi, Mai Ha Hoang, Tien Dat Doan; investigation, Hong Tham Nguyen, Duc Long Tran, Giang Le Nhat Thuy; data analysis, Nhung Hac Thi, Hong Tham Nguyen, Ho Thi Oanh; project administration, Mai Ha Hoang; validation, Ha Tran Nguyen; writing – original draft, Nhung Hac Thi; writing – review & editing, Mai Ha Hoang, Tuyen Van Nguyen, and Nhung Hac Thi. All authors have read and agreed to the published version of the manuscript.

Conflicts of interest

There are no conflicts of interest to declare.

Data availability

The data supporting this article have been included as part of the Supplementary Information (SI). Supplementary information is available. See DOI: https://doi.org/10.1039/d5ra07990j.

Acknowledgements

This research is funded by Vietnam Academy of Science and Technology under grant number KHCBHH.02/24-25. Nhung Hac Thi acknowledges financial support by the PhD Scholarship Programme of Vingroup Innovation Foundation (Code VINIF.2024.TS.025).

References

1 Q. Li, X. Li and Y. Meng, *Thermochim. Acta*, 2012, **549**, 69–80.
2 F.-L. Jin, X. Li and S.-J. Park, *J. Ind. Eng. Chem.*, 2015, **29**, 1–11.
3 S. Kumar, S. Krishnan, S. Mohanty and S. K. Nayak, *Polym. Int.*, 2018, **67**, 815–839.
4 J. Li, H. Zhao and G. Sui, *RSC Adv.*, 2022, **12**, 31699–31710.
5 B. Xu, L. Shao, J. Wang, Y. Liu and L. Qian, *Polym. Degrad. Stab.*, 2020, **181**, 109281.
6 Y. Sui, X. Dai, P. Li and C. Zhang, *Macromol. Mater. Eng.*, 2021, **306**, 100239.
7 Y. Sui, X. Dai, P. Li and C. Zhang, *Eur. Polym. J.*, 2021, **156**, 110601.
8 Y. Sui, H. Sima, W. Shao and C. Zhang, *Composites, Part B*, 2022, **229**, 109463.
9 Y. He, X. Cui, Z. Liu, F. Lan, J. Sun, H. Li, X. Gu and S. Zhang, *Polym. Degrad. Stab.*, 2023, **218**, 110579.
10 X. Chen, Y. Ma, S. Liu, A. Zhang, W. Liu and S. Huang, *Adv. Ind. Eng. Polym. Res.*, 2025, **8**, 48–62.
11 B. Yuan, A. Fan, M. Yang, X. Chen, Y. Hu, C. Bao, S. Jiang, Y. Niu, Y. Zhang, S. He and H. Dai, *Polym. Degrad. Stab.*, 2017, **143**, 42–56.
12 G. Turgut, M. Dogan, U. Tayfun and G. Ozkoc, *Polym. Degrad. Stab.*, 2018, **149**, 96–111.
13 S. Khanal, Y. Lu, S. Ahmed, M. Ali and S. Xu, *Polym. Test.*, 2020, **81**, 106177.
14 Y. Zhan, X. Wu, S. Wang, B. Yuan, Q. Fang, S. Shang, C. Cao and G. Chen, *Polym. Degrad. Stab.*, 2021, **191**, 109684.
15 F. N. Nguyen and J. C. Berg, *Compos. Appl. Sci. Manuf.*, 2008, **39**, 1007–1011.
16 F. N. Nguyen, A. M. Saks and J. C. Berg, *J. Adhes. Sci. Technol.*, 2007, **21**, 1375–1393.
17 M. Liao, H. Chen, L. Deng, X. Wei, Z. Zou, H. Wang, S. Chen and Z. Zhu, *React. Funct. Polym.*, 2023, **192**, 105735.
18 S. Wang and R. Ma, *J. Appl. Polym. Sci.*, 2025, **142**, 56807.
19 R. Ma and S. Wang, *J. Appl. Polym. Sci.*, 2025, **142**, 57554.
20 K. Wu, Z. Wang and H. Liang, *Polym. Compos.*, 2008, **29**, 854–860.
21 K. Wu and Z. Wang, *Polym.-Plast. Technol. Eng.*, 2008, **47**, 247–254.
22 G. Tang, H. Jiang, Y. Yang, D. Chen, C. Liu, P. Zhang, L. Zhou, X. Huang, H. Zhang and X. Liu, *J. Polym. Res.*, 2020, **27**, 375.
23 K. Wu, L. Song, Z. Wang and Y. Hu, *J. Polym. Res.*, 2008, **16**, 283–294.
24 K. Wu, L. Song, Z. Wang and Y. Hu, *Polym. Adv. Technol.*, 2008, **19**, 1914–1921.
25 K. Wu, Z. Wang and Y. Hu, *Polym. Adv. Technol.*, 2008, **19**, 1118–1125.
26 W. Wang, W. Zhang, S. Zhang and J. Li, *Constr. Build. Mater.*, 2014, **65**, 151–158.
27 T. T. Nguyen Thanh, Z. Yusifov, B. Tóth, K. Bocz, P. Márton, Z. Hórvölgyi, G. Marosi and B. Szolnoki, *Fire*, 2024, **7**, 97.
28 L. Feng, K. Y. Wang, J. Willman and H. C. Zhou, *ACS Cent. Sci.*, 2020, **6**, 359–367.
29 Q. Zhang, S. Yan, X. Yan and Y. Lv, *Sci. Total Environ.*, 2023, **902**, 165944.
30 R. Ncube, M. Ghodrat and J. P. Escobedo-Diaz, *Polym. Degrad. Stab.*, 2025, **242**, 111643.
31 G. Huang, Y.-T. Pan, L. Liu, P. Song and R. Yang, *Adv. Nanocompos.*, 2025, **2**, 1–14.
32 R. Ma, Y. Hou, W. Zhang, Y.-T. Pan, S. Huo and C. Shi, *Adv. Compos. Hybrid Mater.*, 2025, **8**, 351.
33 J. Li, H. Zhao, H. Liu, J. Sun, J. Wu, Q. Liu, Y. Zheng and P. Zheng, *RSC Adv.*, 2023, **13**, 22639–22662.
34 X. Sun, Y.-T. Pan, W. Wang and R. Yang, *RSC Appl. Interfaces*, 2025, **2**, 14–24.
35 Y. Hou, W. Hu, Z. Gui and Y. Hu, *Compos. Sci. Technol.*, 2017, **152**, 231–242.
36 Y.-T. Pan, J. Wan, X. Zhao, C. Li and D.-Y. Wang, *Chem. Eng. J.*, 2017, **330**, 1222–1231.
37 B. Xu, W. Xu, Y. Liu, R. Chen, W. Li, Y. Wu and Z. Yang, *Polym. Adv. Technol.*, 2018, **29**, 2816–2826.
38 W. Guo, S. Nie, E. N. Kalali, X. Wang, W. Wang, W. Cai, L. Song and Y. Hu, *Composites, Part B*, 2019, **176**, 107261.
39 M. Zhang, X. Ding, Y. Zhan, Y. Wang and X. Wang, *J. Hazard. Mater.*, 2020, **384**, 121260.
40 W. Xu, G. Wang, J. Xu, Y. Liu, R. Chen and H. Yan, *J. Hazard. Mater.*, 2019, **379**, 120819.
41 X. L. Qi, D. D. Zhou, J. Zhang, S. Hu, M. Haranczyk and D. Y. Wang, *ACS Appl. Mater. Interfaces*, 2019, **11**, 20325–20332.
42 J. Cao, S. Chen, Z. Han, Y.-T. Pan, Y. Lin, W. Wang and R. Yang, *Chem. Eng. J.*, 2024, **501**, 157758.
43 Q. Li, Y. Lei, X. Bi, Y. Liu, Y.-T. Pan, W. Wang, W. Zhang, C. Shi and G. H. Yeoh, *Chem. Eng. J.*, 2025, **506**, 160242.
44 Y. Yang, D.-Y. Wang, R.-K. Jian, Z. Liu and G. Huang, *Prog. Org. Coat.*, 2023, **175**, 107316.
45 Hexion Specialty Chemicals, Technical Information of Epikote Resin MGS LR 385, https://www.swiss-composite.ch/pdf/t-L-385-e.pdf, accessed November, 2025.

46 Hexion, Safety Data Sheet of EPIKURE ™ Curing Agent MGS LH 386, https://www.swiss-composite.ch/pdf/s-EPIKURE-Curing-Agent-MGS-LH-386-e.pdf, accessed November, 2025.

47 A. D. S. Barbosa, D. Julião, D. M. Fernandes, A. F. Peixoto, C. Freire, B. de Castro, C. M. Granadeiro, S. S. Balula and L. Cunha-Silva, *Polyhedron*, 2017, **127**, 464–470.

48 K. Vinothkumar and R. G. Balakrishna, *Appl. Catal., B*, 2024, **340**, 123199.

49 L. Meng, Z. Zhang, M. Ju, J. Xu and Z. Wang, *Int. J. Energy Res.*, 2022, **46**, 23480–23492.

50 B. Liu, X. Gao, Y. Zhao, L. Dai, Z. Xie and Z. Zhang, *J. Mater. Sci.*, 2017, **52**, 8603–8617.

51 X.-X. Zheng, L.-J. Shen, X.-P. Chen, X.-H. Zheng, C.-T. Au and L.-L. Jiang, *Inorg. Chem.*, 2018, **57**, 10081–10089.

52 S.-W. Lv, J.-M. Liu, C.-Y. Li, N. Zhao, Z.-H. Wang and S. Wang, *Chem. Eng. J.*, 2019, **375**, 122111.

53 T. Zhang and Y. Liu, *Polymers*, 2023, **15**, 4665.

54 P. Mishra, A. Behera, D. Kandi and K. Parida, *Nanoscale Adv.*, 2019, **1**, 1864–1879.

55 Z. Zhang, D. Kong, H. Sun, L. Sun, C. Dong and Z. Lu, *Cellulose*, 2020, **27**, 10473–10487.

56 S. J. Kashyap, R. Sankannavar and G. M. Madhu, *Mater. Chem. Phys.*, 2022, **286**, 126118.

57 K. Yang, H. Peng, Y. Wen and N. Li, *Appl. Surf. Sci.*, 2010, **256**, 3093–3097.

58 Y. Liu, Z. Li, Y. You, X. Zheng and J. Wen, *RSC Adv.*, 2017, **7**, 51281–51289.

59 Y. Wang, Y. Wang, S. Luo, M. Jiang, C. Liu, F. Teng, H. Chen, H. Shen and D. Gao, *Ionics*, 2019, **26**, 1645–1655.

60 Z. B. S. Y. Tan, X. F. Chen, J. W. Long, L. Chen and Y. Z. Wang, *ACS Appl. Mater. Interfaces*, 2015, **7**, 17919–17928.

61 Z.-B. Shao, C. Deng, Y. Tan, M.-J. Chen, L. Chen and Y.-Z. Wang, *Polym. Degrad. Stab.*, 2014, **106**, 88–96.

62 Z.-B. Shao, C. Deng, Y. Tan, M.-J. Chen, L. Chen and Y.-Z. Wang, *ACS Appl. Mater. Interfaces*, 2014, **6**, 7363–7370.

63 Z.-B. Shao, C. Deng, Y. Tan, L. Yu, M.-J. Chen, L. Chen and Y.-Z. Wang, *J. Mater. Chem. A*, 2014, **2**, 13955.

64 W. Yan, J. Yu, M. Zhang, S. Qin, T. Wang, W. Huang and L. Long, *RSC Adv.*, 2017, **7**, 46236–46245.

65 N. Thi, T. Doanh, H. Nguyen, H. Oanh, T. Doan and M. H. Hoang, *J. Appl. Polym. Sci.*, 2025, e57993.

66 S. D. Alexandratos and X. Zhu, *Vib. Spectrosc.*, 2018, **95**, 80–89.

67 J. S. Wang, D. Y. Wang, Y. Liu, X. G. Ge and Y. Z. Wang, *J. Appl. Polym. Sci.*, 2008, **108**, 2644–2653.

68 S. Wang, Q. Fang, C. Liu, J. Zhang, Y. Jiang, Y. Huang, M. Yang, Z. Tan, Y. He, B. Ji, C. Qi and Y. Chen, *Eur. Polym. J.*, 2023, **187**, 111897.

69 Y. Zhang, Y. Zheng, H. Geng, Y. Yang, M. Ye, Y. Zhang and C. Li, *Chem.–Eur. J.*, 2021, **27**, 9031–9037.

70 Y. Tan, Z.-B. Shao, L.-X. Yu, Y.-J. Xu, W.-H. Rao, L. Chen and Y.-Z. Wang, *Polym. Degrad. Stab.*, 2016, **131**, 62–70.